# High-Speed Bolometry Based on Johnson Noise Detection of Hot Electrons in Cavity-Coupled Graphene

D. K. Efetov [1,2], R.-J. Shiue [1], Y. Gao [3], B. Skinner [4], E. Walsh [1], H. Choi [1], J. Zheng [1], C. Tan [3], G. Grosso [1], C. Peng [1], J. Hone [3], K. C. Fong [5] and D. Englund [1]

1. Department of Electrical Engineering and Computer Science, Massachusetts Institute of Technology, Cambridge MA 02139
2. ICFO - Institut de Ciencies Fotoniques, The Barcelona Institute of Science and Technology, 08860 Castelldefels, Barcelona, Spain
3. Department of Mechanical Engineering, Columbia University, New York NY 10027
4. Department of Physics, Massachusetts Institute of Technology, Cambridge MA 02139
5. Raytheon BBN Technologies, Quantum Information Processing Group, Cambridge, Massachusetts 02138, USA

**Since the invention of the bolometer, its main design principles relied on efficient light absorption into a low-heat-capacity material and its exceptional thermal isolation from the environment. While the reduced thermal coupling to its surroundings allows for an enhanced thermal response, it in turn strongly reduces the thermal time constant and dramatically lowers the detector's bandwidth. With its unique combination of a record small electronic heat capacity and a weak electron-phonon coupling, graphene has emerged as an extreme bolometric medium that allows for both, high sensitivity and high bandwidths. Here, we introduce a hot-electron bolometer based on a novel Johnson noise readout of the electron gas in graphene, which is critically coupled to incident radiation through a photonic nanocavity. This proof-of-concept operates in the telecom spectrum, achieves an enhanced bolometric response at charge neutrality with a noise equivalent power NEP < 5pW/√Hz, a thermal relaxation time of $\tau$ < 34ps, an improved light absorption by a factor ~3, and an operation temperature up to T=300K.**

High sensitivity and fast response are the most important metrics for infrared sensing and imaging and together form the primary tradeoff space in bolometry [1]. To simultaneously improve both characteristics requires a paradigm shift on the thermal properties of bolometric materials. Due to a vanishingly small density of states (DOS) at the charge neutrality point (CNP)[2,3], graphene has a record-low electronic heat capacity which can reach values approaching one Boltzmann constant $C_e \sim k_b$ [4–6]. In addition, its small Fermi surface and the high energy of its phonons result in an extremely weak electron-phonon (e-ph) heat exchange[7–9]., The combination will allow a strong thermal isolation of the electrons in graphene for higher sensitivity without sacrificing the detector response time. These unique thermal properties and its broadband photon absorption[10], make graphene a promising platform for ultrasensitive and ultra-fast hot electron bolometers, calorimeters and single photon detectors for low energy light[11–13].

While there already have been device concepts demonstrating bolometric response of graphene [14–16], many challenges remain on the way to practical applications, like the very low light absorption of only 2.3%[10] and low measurement bandwidths. Previous work

utilized straightforward transport techniques in order to achieve high bolometric response $\Delta T_e$, employing the devices' temperature dependent resistance $R(T_e)$. However, in order to get high bolometric sensitivities, the very weak $\Delta R(T_e)/\Delta T_e$ of intrinsic graphene had to be artificially increased by introducing disorder[17], patterning nanostructures[18], or opening a band gap in bilayer graphene[14]. The fundamental challenge in this approach is set by the enormous impedance mismatch between these high impedance devices, with both - free space[19,20] and the readout circuit, which consequently results in very low light coupling efficiencies and readout bandwidths, accordingly. To overcome this issue and achieve all at the same time - high bolometric sensitivity, high readout bandwidth and efficient light absorption, it is necessary to introduce a $T_e$ readout scheme that works for high-quality, low impedance graphene and to couple the bolometer to resonant light structures.

In this manuscript we present a new graphene bolometer device concept based on a Johnson noise radiometry (JNR) readout and resonant coupling to a photonic crystal nanocavity. Since graphene's electrons have a weak coupling to the environment through electronic diffusion [6,21] and e-ph coupling [5,7,9], absorbed radiation gives rise to a $T_e$ that can be dramatically higher than its environment (Fig. 1(a)). As is given by the Johnson-Nyquist theorem, these thermally agitated electrons emit noise at microwave frequencies with a power that is directly proportional to $T_e$, which hence allows for a direct and universal $T_e$ readout[5,6,21]. Such an approach does not require large $\Delta R(T_e)/\Delta T_e$ dependence and enables the use of ultra-high mobility graphene samples. It allows critical coupling to incident radiation through integration into resonant structures, avoids performance limiting self heating effects, and sets no hard limit to the operation temperature T of the detector.

Fig. 1 (b) shows the device schematics and operation principle of the bolometer. A high quality graphene/hexagonal boron nitride heterostructure (hBN/G/hBN) is integrated onto a suspended silicon L3 photonic crystal cavity (PCC). The resonant cavity mode of the PPC (Fig. 1 (c)) is critically coupled to the telecom spectrum and evanescently overlaps with the graphene sheet. To maximize heat generation and to minimize heat dissipation, the graphene stack is etched into a circle with $5\,\mu m$ diameter, corresponding to the expected cooling lengths, and is connected to gold leads with narrow, resistive graphene channels. Through the gold leads, the device is impedance matched to a LC network (50 Ω) with a resonant frequency at ~ 70 MHz and a bandwidth of ~ 20 MHz (SI), and is further connected to a low noise amplifier (LNA) and a heterodyne circuit at room temperature, which together form the JNR readout scheme.

The device is probed at a cryogenic temperature T=5K with a tunable near-IR laser which is normally coupled to the PPC through a cross-polarized confocal scanning setup. Simultaneously to spatial scanning of the laser pulses, we read out the calibrated JNR signal with a lock-in amplifier and obtain $\Delta T_e$, the increase of $T_e$. Fig. 1 (d) left shows the optical image of the device and Fig. 1 (e) the typical $\Delta T_e$ spatial maps under linearly polarized light at the PPCs resonant frequency of 1532 nm and an absorbed laser power of P=380 nW. As the PPC resonant mode only couples to light with polarization along the x-axis, we can compare the response off ($90^0$ polarization) and on ($0^0$ polarization) resonance (Fig. 1 (e) left and middle). When off resonance, the response comes mostly from the entire graphene

region, while when on resonance it is strongly enhanced in the cavity region of the PPC. Assuming the thermal model in Fig. 1 (a), we theoretical model the response map (SI) and find good qualitative matching with the experimental findings (Fig. 1 (e) right). The response is generated only when the laser is incident onto the graphene, confirming that the JNR readout is primarily sensitive to thermal noise inside the graphene channel and nowhere else in the circuit.

To characterize the enhancement of light absorption by the PPC we perform measurements of the reflection spectrum of the irradiated cavity before the deposition of the hBN/G/hBN stack and after. Fig. 2 (a) shows the fundamental mode of the pure cavity with a resonance mode at 1512.8nm with a quality factor of *Q* ~ 7000. After the hBN/G/hBN deposition, the cavity resonance is red-shifted to 1531.7 nm and its *Q* drops to ~ 900. Here the shift of the mode is mainly due to hBN's high dielectric constant of ~3.9, while its' broadening is caused by the light absorption in the graphene. From coupled mode theory[22], we can estimate that the total absorption of the cavity resonant field into graphene is ~ 45%.

The enhanced light absorption amplifies the photoresponse. Fig. 2 (b) shows $\Delta T_e$ as a function of incident laser wavelength for $0^0$ (on) and $90^0$ (off) polarized light with respect to the cavity x-axis (Fig. 1(c)). In the on state at resonance wavelength of 1531.7nm, $\Delta T_e$ is enhanced by a factor of ~3 and follows a sinusoidal dependence as a function of the polarization angle (Fig. 2(b) inset). By comparing the response at the on and off polarization states, the total absorption in graphene is enhanced from 2.3% of single-pass vertical incidence to ~ 7% in the PPC cavity. Since graphene absorbs ~ 45% of the cavity field at normal incidence, we extract a coupling efficiency of the cavity field to the normal incidence to be ~ 10%, consistent with simulation results. With improved fabrication however, one can expect near-unity absorption in graphene via the nanocavity field. Here through critical coupling to a waveguide[23,24] or free-space[25,26], light coupling can be dramatically increased to ~ 99%, and experimentally >90% absorption from a photonic nanocavity into graphene has already been demonstrated[22].

We now probe $\Delta T_e$ as a function of absorbed laser power P at T=5K (Fig. 3 (a)). Here the response transitions from a linear to a sublinear dependence with increased P, and is overall strongly reduced at elevated temperatures (inset Fig. 3(a)). We can model this behaviour with the 2D heat transfer equation below (Eq. 1), which takes into account the two main dissipation mechanisms : electronic dissipation through the WF law (first term) and e-ph interaction (second term) :

$$\dot{q} = -\vec{\nabla}\cdot[\kappa\vec{\nabla}T_e] + \Sigma_{ep}[{T_e}^3 - T^3] \text{ , (Eq. 1)}$$

where $\Sigma_{ep}$ is the e-ph coupling strength, T the lattice temperature, $\kappa = \frac{\pi^2}{3}(\frac{k}{e\rho})T_e$ the thermal conductivity, k the Boltzmann constant, and ρ the resistivity, which is extracted from transport measurements (see SI for more details). Numerical modeling with only one fitting parameter $\Sigma_{ep} = 0.038\ W/(m^2K^3)$ produces a good match with the experiment and agrees well with previously reported values[6]. We can qualitatively understand the sub-linear behaviour by the overall enhancement of the electronic thermal conductivity $G_{th}$ at higher T, where both, WF, and e-ph dissipation channels are strongly enhanced. The bolometric

response due to laser heating is furthermore well consistent with that through Joule heating[5] (Fig. 3(a)), and minor deviations can be attributed to saturable light absorption in graphene at high laser powers[27].

Ultimately, the continuous wave bolometric response is limited by the electronic thermal conductivity $G_{th}$ through the simple relation $\Delta T_e = P/G_{th}$, which is a direct consequence of Eq. 1. From measurements at various T with a fixed P=200nW, we obtain the $G_{th}(T)$ dependence (Fig. 3 (b)). It is overall in good agreement with our heat dissipation model, and follows a linear WF dependence at low T and a power law e-ph dependence at higher T. Since both $C_e$ and $G_{th}$ are expected to be strongly reduced at small carrier densities n[6], we test $\Delta T_e$ as a function of n by applying a gate voltage $V_{bg}$ to the PPC. Fig. 3 (c) plots $\Delta T_e(V_{bg})$ for P=10nW and $R(V_{bg})$ (both taken at T=5K). This enhancement sharply increases with a factor ~3 at the CNP and qualitatively follows the same dependence as $R(V_{bg})$. However this enhancement is predicted to be several orders of magnitude higher at mK temperatures[5,13].

The non-linear $\Delta T_e(P)$ in Fig. 3 (a) enables us to test the thermal relaxation time of the electrons $\tau$, which defines the ultimate reset time of the detector. Instead of continuous wave laser excitation, we probe the system with two time delayed pulses[28–30] (FWHM of 250fs) and a repetition rate of 78MHz. Fig. 4 (a) shows the normalized JN power (JNP) as a function of the delay time between the two pulses, JNP(0ps)/JNP(120ps). The signal shows a strong time dependence, with a pronounced dip at 0ps and an increased signal at higher absolute delay times, where it follows an inverse exponential form and saturates. From the half-width-half-maximum (HWHM) of the central dip structure we can deduce the intrinsic relaxation time of the hot electrons $\tau$ for each T, which are in good agreement with similar studies of the photothermoelectric effect in graphene [14,28–32]

From all these measurements, we can now extract the device performance given by the detector noise equivalent power NEP and reset time $\tau$ (Fig. 4 (a)). Calibration of the bolometric readout scheme gives an overall temperature sensitivity of $\delta T=5mK/Hz^{1/2}$ (SI), which together with the $G_{th}$ values from Fig. 3 (b) allows to extract the NEP of the bolometer. Unlike in the case of bolometers with a resistive readout, JNR does not have a hard limit on the operation temperature and can be operated above liquid nitrogen temperature and even at room temperature. Here we find an NEP ~ 5 $pW/Hz^{1/2}$ and $\tau$ ~ 34ps at T=5K, NEP ~ 17 $pW/Hz^{1/2}$ and $\tau$ ~ 14ps at T=100K, and NEP ~ 150 $pW/Hz^{1/2}$ and $\tau$ ~ 6ps at T=300K.

As is given by the Dicke radiometer relation[33], the temperature sensitivity of the system is given by $\delta T=(T_e+T_s)/(Bt)^{1/2}$, where $T_s$ is the system noise, B is the measurement bandwidth and t the total measurement time. From comparison with the experimentally observed δT we find that the sensitivity in our measurement is significantly limited by $T_s$. It can however be dramatically reduced by cooling the entire measurement circuit and the use of quantum limited amplifiers, and it was shown theoretically that the presented device concept can reach a NEP < $10^{-20}$ $W/Hz^{1/2}$ at T=10mK [13]. The ultimate speed of the readout electronics has also no hard limit and it is feasible to reach the intrinsic detector reset times $\tau$ ~10 ps, which corresponds to a maximal bandwidth of B~30 GHz. As follows from the Dicke relation

a faster readout would sacrifice the measurement sensitivity (SI), but it would have no effect on the NEP. Another point which needs attention is the loss of graphene's broadband absorption properties through the integration of the bolometer into resonant light structures. It is however feasible that future applications would use bolometer arrays that are individually coupled to different resonant frequencies, so making it sensitive to a broad range of frequencies.

Altogether this shows that our proof-of-concept device can be a promising bolometer with efficient light absorption and a superior sensitivity-bandwidth product. Since the detector also has no limitations on its operation temperature, it provides engineering flexibility, which overall opens a new route for practical applications in the fields of thermal imaging, observational astronomy, quantum information and quantum sensing. In particular, since it is more than 5 times faster than the bandwidth of the intermediate frequency in the hot electron bolometer mixer[34], it can be employed as a cutting edge bolometric mixer material.

Acknowledgements:

We thank Leonid Levitov, Dan Prober and Frank Koppens for fruitful discussions. D.K.E. acknowledges support from the MIT EFRC Excitonics Center, the Cellex Foundation and Excelencia Severo Ochoa. Y.G. and J.H. acknowledge support from the US Office of Naval Research N00014-13-1-0662. K.C.F. acknowledges support from Raytheon BBN Technologies. This work is supported in part by the Semiconductor Research Corporation's NRI Center for Institute for Nanoelectronics Discovery and Exploration (INDEX).

[1] P. L. Richards, J. Appl. Phys. **76**, 1 (1994).
[2] A. H. Castro Neto, F. Guinea, N. M. R. Peres, K. S. Novoselov, and A. K. Geim, Rev. Mod. Phys. **81**, 109 (2009).
[3] S. Das Sarma, S. Adam, E. H. Hwang, and E. Rossi, Rev. Mod. Phys. **83**, 407 (2011).
[4] A. A. Balandin, Nat. Mater. **10**, 569 (2011).
[5] K. C. Fong and K. C. Schwab, Phys. Rev. X **2**, 031006 (2012).
[6] K. C. Fong, E. E. Wollman, H. Ravi, W. Chen, A. A. Clerk, M. D. Shaw, H. G. Leduc, and K. C. Schwab, Phys. Rev. X **3**, 041008 (2013).
[7] D. K. Efetov and P. Kim, Phys. Rev. Lett. **105**, 256805 (2010).
[8] W.-K. Tse and S. Das Sarma, Phys. Rev. B Condens. Matter **79**, 235406 (2009).
[9] A. C. Betz, F. Vialla, D. Brunel, C. Voisin, M. Picher, A. Cavanna, A. Madouri, G. Fève, J.-M. Berroir, B. Plaçais, and E. Pallecchi, Phys. Rev. Lett. **109**, 056805 (2012).
[10] K. F. Mak, M. Y. Sfeir, Y. Wu, C. H. Lui, J. A. Misewich, and T. F. Heinz, Phys. Rev. Lett. **101**, 196405 (2008).
[11] E. D. Walsh, D. K. Efetov, G.-H. Lee, M. Heuck, J. Crossno, T. A. Ohki, P. Kim, D. Englund, and K. C. Fong, Phys. Rev. Applied **8**, 024022 (2017).
[12] X. Du, D. E. Prober, H. Vora, and C. B. Mckitterick, Graphene and 2D Materials **1**, (n.d.).
[13] C. B. McKitterick, D. E. Prober, and B. S. Karasik, J. Appl. Phys. **113**, 044512 (2013).
[14] J. Yan, M.-H. Kim, J. A. Elle, A. B. Sushkov, G. S. Jenkins, H. M. Milchberg, M. S. Fuhrer, and H. D. Drew, Nat. Nanotechnol. **7**, 472 (2012).
[15] H. Vora, P. Kumaravadivel, B. Nielsen, and X. Du, Appl. Phys. Lett. **100**, 153507 (2012).
[16] X. Cai, A. B. Sushkov, R. J. Suess, M. M. Jadidi, G. S. Jenkins, L. O. Nyakiti, R. L. Myers-Ward, S. Li, J. Yan, D. K. Gaskill, T. E. Murphy, H. D. Drew, and M. S. Fuhrer, Nat. Nanotechnol. **9**, 814 (2014).
[17] Q. Han, T. Gao, R. Zhang, Y. Chen, J. Chen, G. Liu, Y. Zhang, Z. Liu, X. Wu, and D. Yu,

Sci. Rep. **3**, 3533 (2013).
[18] A. El Fatimy, R. L. Myers-Ward, A. K. Boyd, K. M. Daniels, D. K. Gaskill, and P. Barbara, Nat. Nanotechnol. **11**, 335 (2016).
[19] U. Sassi, R. Parret, S. Nanot, M. Bruna, S. Borini, D. De Fazio, Z. Zhao, E. Lidorikis, F. H. L. Koppens, A. C. Ferrari, and A. Colli, Nat. Commun. **8**, 14311 (2017).
[20] Y. Zhou, Y. E, L. Zhu, M. Qi, X. Xu, J. Bai, Z. Ren, and L. Wang, Carbon N. Y. **96**, 1129 (2016).
[21] J. Crossno, J. K. Shi, K. Wang, X. Liu, A. Harzheim, A. Lucas, S. Sachdev, P. Kim, T. Taniguchi, K. Watanabe, T. A. Ohki, and K. C. Fong, Science **351**, 1058 (2016).
[22] X. Gan, K. F. Mak, Y. Gao, Y. You, F. Hatami, J. Hone, T. F. Heinz, and D. Englund, Nano Lett. **12**, 5626 (2012).
[23] R.-J. Shiue, X. Gan, Y. Gao, L. Li, X. Yao, A. Szep, D. Walker Jr, J. Hone, and D. Englund, Appl. Phys. Lett. **103**, 241109 (2013).
[24] H. Takano, B. S. Song, T. Asano, and S. Noda, Opt. Express **14**, 3491 (2006).
[25] J. Zheng, R. A. Barton, and D. Englund, ACS Photonics **1**, 768 (2014).
[26] J. R. Piper and S. Fan, ACS Photonics **1**, 347 (2014).
[27] A. Marini, J. D. Cox, and F. J. G. de Abajo, arXiv [cond-Mat.mes-Hall] (2016).
[28] K. J. Tielrooij, L. Piatkowski, M. Massicotte, A. Woessner, Q. Ma, Y. Lee, K. S. Myhro, C. N. Lau, P. Jarillo-Herrero, N. F. van Hulst, and F. H. L. Koppens, Nat. Nanotechnol. **10**, 437 (2015).
[29] M. W. Graham, S.-F. Shi, D. C. Ralph, J. Park, and P. L. McEuen, Nat. Phys. **9**, 103 (2012).
[30] R.-J. Shiue, Y. Gao, Y. Wang, C. Peng, A. D. Robertson, D. K. Efetov, S. Assefa, F. H. L. Koppens, J. Hone, and D. Englund, Nano Lett. **15**, 7288 (2015).
[31] K. J. Tielrooij, N. C. H. Hesp, A. Principi, M. Lundeberg, E. A. A. Pogna, L. Banszerus, Z. Mics, M. Massicotte, P. Schmidt, D. Davydovskaya, K. Watanabe, T. Taniguchi, M. Bonn, D. Turchinovich, C. Stampfer, G. Cerullo, M. Polini, and F. H. L. Koppens, arXiv [cond-Mat.mes-Hall] (2017).
[32] D. Sun, G. Aivazian, A. M. Jones, J. S. Ross, W. Yao, D. Cobden, and X. Xu, Nat. Nanotechnol. **7**, 114 (2012).
[33] R. H. Dicke, Rev. Sci. Instrum. **17**, 268 (1946).
[34] A. Shurakov, Y. Lobanov, and G. Goltsman, Supercond. Sci. Technol. **29**, 023001 (2015).

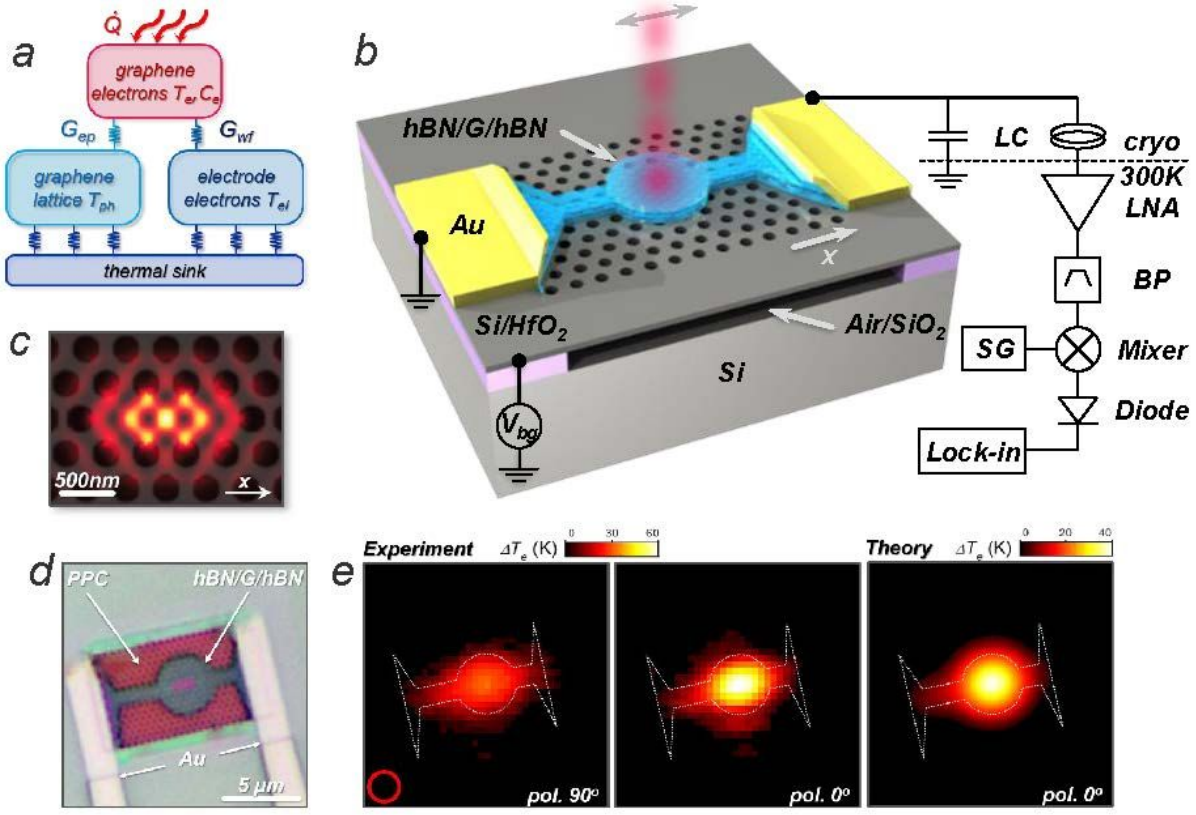


**Figure 1: Device schematics and operation principle.** (a) Schematics of heat dissipation channels of irradiated hot electrons in graphene. Primary mechanism includes the WF law ($G_{WF}$) and e-ph scattering ($G_{ep}$). (b) Schematic of the device, which consists of a side contacted hBN/G/hBN heterostructure on top of a suspended silicon L3 PPC. The device is impedance matched to a LC network at cryogenic temperatures and is read out by a heterodyne JNR thermometry scheme at room temperature, which allows for an accurate reading of $T_e$. (c) Resonant modes form in the L3 PPC as is seen in the calculated spatial electric field intensity $|E|^2$ profile. (d) Optical microscope image of the device. (e) Map of the bolometric response of the device as a function of laser position (red circle – laser spot size). Left: $\Delta T_e$ for $90^0$ polarized light (PPC off resonance), middle: for $0^0$ polarized light (PPC on resonance) and right: theoretical model for $0^0$ polarized light. Overall the bolometric response occurs only when the laser beam is injected on the graphene covered area, which is strongly enhanced when the PPC mode is on resonance.

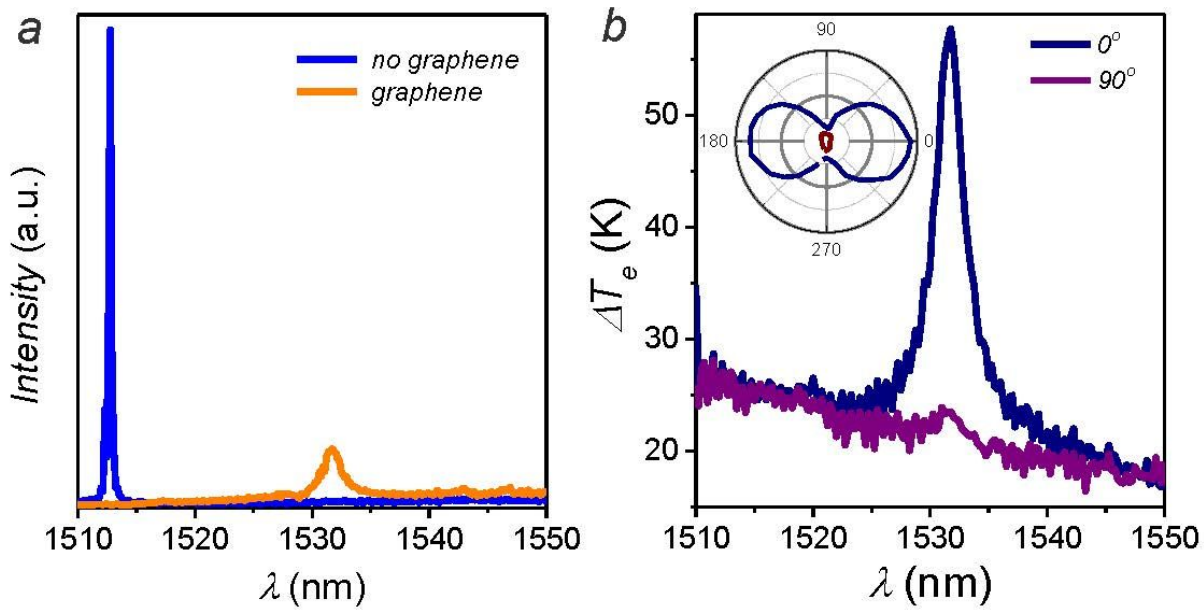


**Figure 2: Role of the PPC – enhancement of the bolometric response.** (a) Reflection spectra of the normally excited PPC cavity mode before and after the deposition of the hBN/G/hBN stack. Due to light absorption in the graphene the resonance is broadened and red-shifted. (b) Bolometric response as a function of the incident wavelength for $0^0$ (on) and $90^0$ (off) polarized light. Inset shows sinusoidal polarization angle dependence of $\Delta T_e$ for different wavelengths on (blue) and off (red) resonance.

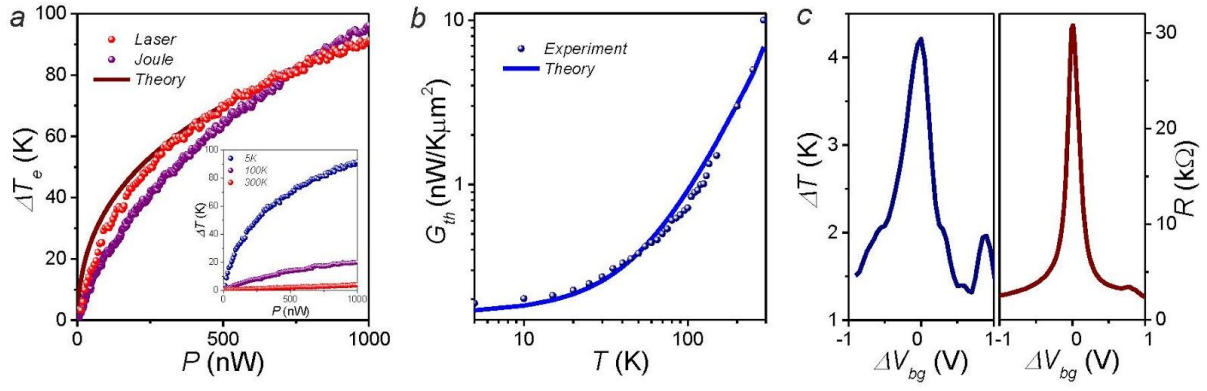


**Figure 3: Bolometric response.** (a) Bolometric response $\Delta T_e$ as a function of absorbed heating power P for laser and Joule heating. Inset shows the bolometric response at various device temperatures T. (b) The extracted thermal conductance $G_{th}=P/\Delta T_e$ per device area as a function of T. Overall the experimental results in (a) and (b) are consistent with a heat dissipation model based on the WF law and e-ph coupling. The bolometric response is limited by thermally activated dissipation mechanisms and is strongly reduced at elevated T. (c) Gate dependence of $\Delta T_e(V_{bg})$ at P=10nW (left) and of $R(V_{bg})$ (right), both measured at T=5K. The curves show qualitatively similar dependence with a strong enhancement of $\Delta T_e$ at the CNP.

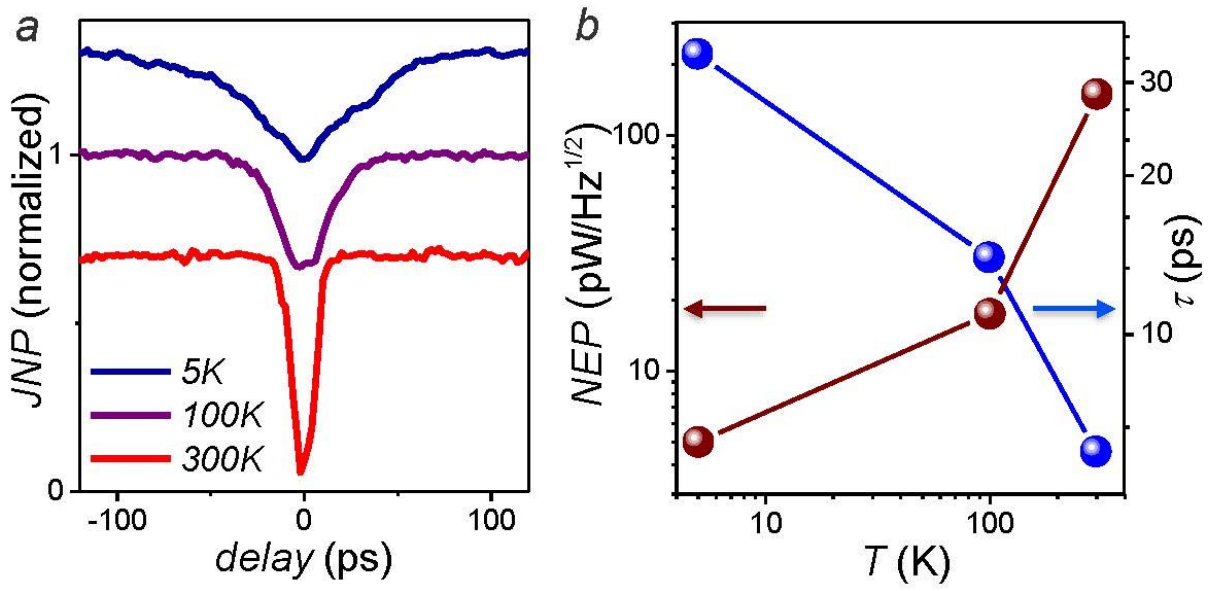


**Figure 4: Detector performance.** (a) Normalized Johnson noise power probed with two delayed laser pulses at various device temperatures T (graphs are offset for clarity). The central dip in the JNP(0ps)/JNP(120ps) signal allows to extract the intrinsic thermal relaxation time of the bolometer $\tau$. As $G_{th}$ becomes reduced at low T, $\tau$ inturn increases from 6ps (300K) to 30ps (5K). (b) NEP and $\tau$ as a function of T. With a NEP ~ 5 pW/Hz$^{1/2}$ and an intrinsic reset time of $\tau$ ~ 34ps at T=5K, the bolometer has an unique combination of high sensitivity and high bandwidth. It has no hard limit on the operation temperature and has a relatively high NEP ~ 150pW/Hz$^{1/2}$ even at room temperature.

# Supplementary information

**S1. Device fabrication**

Graphene/hBN heterostructure:

The hexagonal-boron nitride (hBN)/Graphene/hBN stacks were exfoliated and assembled using a van der Waals assembly technique and then transferred onto the top of the PPC cavity. The total thickness of the two BN layers is around 30 nm. Patterning the BN/Graphene/BN stack with hydrogen-silsesquioxane (HSQ) resist and CHF3+O2 plasma exposes the edges of graphene, which was subsequently contacted by Cr/Pd/Au (1/20/50 nm) metal leads using electron-beam evaporation. Typical device resistance as a function of gate voltage and device temperature is shown in Fig. S1 (a).

Photonic crystal nanocavity:

The PPC cavities were fabricated on a silicon-on-insulator (SOI) wafer using a series of electron-beam lithography (EBL), reactive ion etching, and a wet-etch undercut of the insulator to produce free-standing membranes. The top silicon membrane has a thickness of ~220 nm with a PPC lattice period of a = 440 nm and an air hole radius r = 0.29a. A linear-three-hole (L3) defect in the middle of the PPC lattice serves to form confined optical cavity modes. Finite-difference time-domain (FDTD) simulations shows the fundamental mode of the cavity resonant field (Fig. 1(c)).The fabricated PPC cavity was characterized in a cross-polarized confocal microscope setup with broadband illumination (supercontinuum). The reflection from the cavity was collect and coupled to a spectrometer to analyze its spectrum.

The graphene layer interacts with the cavity through the evanescent field above the subwavelength membrane. The thickness of the membrane plus the thickness of the bottom layer of hBN define the magnitude of the evanescent electric field amplitude at the graphene location. From Lumerical simulations we find it to be ~10% of the field maximum at the center of the structure.

**S2. Johnson noise radiometry**

Impedance matching of the RF circuit:

To achieve impedance matching of the RF circuit and the graphene device we use a LC circuit. It defines a ~20MHz wide band around a resonant frequency of ~70MHz. The challenge is to pick L and C components that allow for a good noise transmission of the noise power through the circuit for all the whole resistance phase space of the device $R(V_{bg}, T)$ as is see in Fig. S1 (b) and (c).

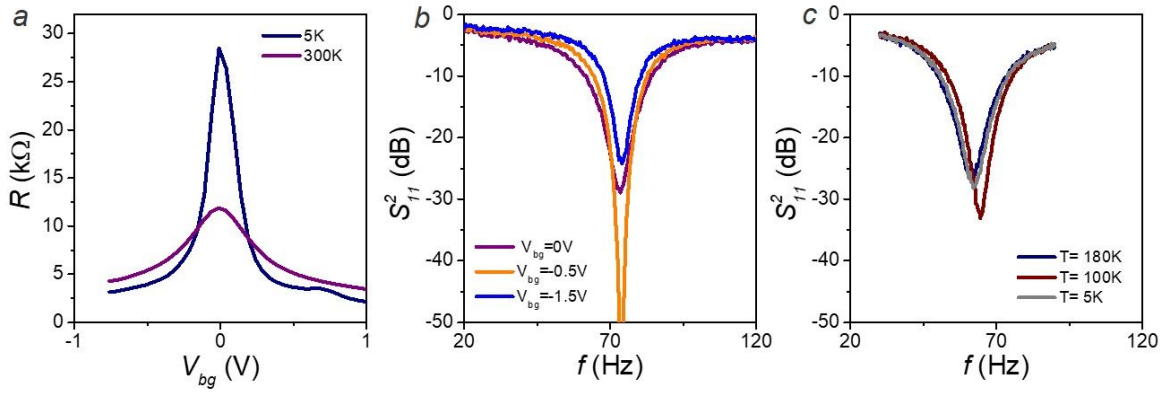


**Figure S1: Resistance and impedance matching of the device.** (a) Two terminal device resistance R as a function of gate voltage $V_{bg}$ for different device temperatures T, show strong T-dependence of the device. (b) Reflectance curves of the RF circuit while tuning the gate voltage $V_{bg}$ of the device at T=5K. (c) Reflectance curves while tuning the device temperature T at $V_{bg}$=0V. (b) and (c) demonstrate good impedance matching for the whole parameter space.

Electronic temperature readout with the JNR:

Fig. S2 (a) shows typical calibration curves for the JNR output voltage as a function of device temperature T. Linear fits to the JNR voltage allow to calibrate the electronic temperature $T_e$ of the electron gas in the graphene bolometer. As the device resistance R changes with gate voltage, it is necessary to calibrate $T_e$ for each gate voltage value separately.

Measurement sensitivity:

In order to estimate the measurement sensitivity we perform more than 1000 independent $T_e$ measurements at T=5K, where we find a measurement uncertainty of $\delta T \sim 5 mK/Hz^{1/2}$ (Fig. S2 (b)). We can fit the δT as a function of the total measurement time t with the Dicke radiometer relation (Fig. S2 (c)).

Time-resolved JNR measurements:

The pulsed laser is generated from an optical parametric oscillator (OPO) pump by a Ti:Sapphire mode-lock laser (Mira-HP, Coherent). The pulse duration is 250 fs with a repetition rate of 78 MHz. The input laser beam was split into two optical arms where one of the arms has a tunable delay relative to the other. The optical pulses were then combined and coupled onto the graphene bolometer via a microscope objective.

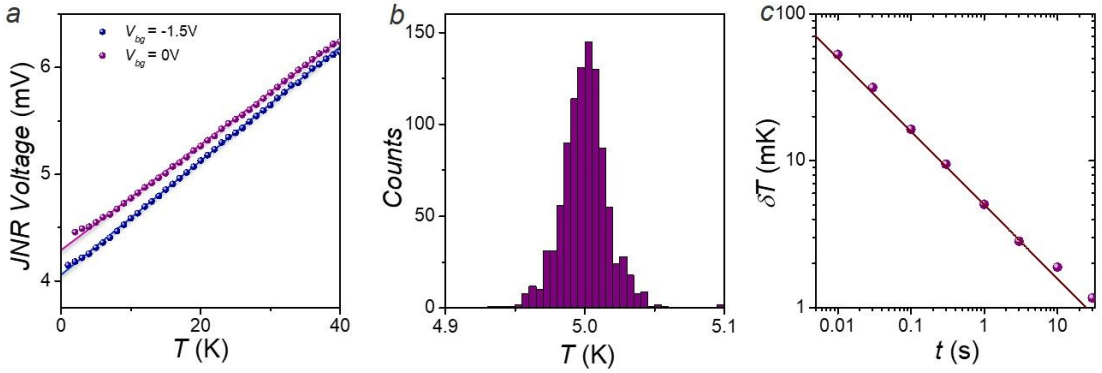


**Figure S2: JNR calibration and sensitivity.** (a) Output JNR voltage is proportional to the integrated noise of device temperature for a fixed device R. The slope of each line gives the $T_e$ calibration for each $V_{bg}$. (b) Histogram of independent $T_e$ using t=1s integration time gives a measurement uncertainty of δT~5mK/Hz$^{1/2}$. (c) The measurement uncertainty δT (bullet points) follows the Dicke relation (fit) for different measurement times t.

**S3. Numerical modeling of Johnson noise temperature**

In order to describe the Johnson noise analytically, we begin from the assumption of a well-defined local electron temperature $T_e(r)$ at a given position r in the sample. This assumption is equivalent to assuming that the electron mean free path (resulting, for example, from scattering by disorder impurities) is much shorter than any of the geometric dimensions of the sample. In this description, each differential area of the sample effectively acts as its own independent noise source and contributes independently to the total Johnson noise measured at the contacts. In particular, the noise current IN can be written

$$I_N = \int [j_N(r) \cdot \nabla \phi(r)] d^2 r \,, \text{(S.1)}$$

where $j_N(r)$ is the local noise current and $\phi(r)$ is a weighting function that obeys the same Laplace equation as the source-drain current[1]. In our problem, $\phi(r)$ is equivalent to the electric potential that results when a unit voltage is applied to the source contact and the drain contact is grounded. Fluctuations to the noise current add in quadrature with each other, $I_N^2 = \int \langle j_N^2(r) \rangle d^2 r$, and since for Johnson noise $\langle j_N^2(r) \rangle \propto T_e(r)$ we arrive at a simple expression for the Johnson noise temperature:

$$T_{JN} = \frac{\int T_e(r)(\nabla \phi)^2 d^2 r}{\int (\nabla \phi)^2 d^2 r} \,. \text{(S.2)}$$

For our device, the function $\phi(r)$ and its spatial gradient can be found numerically using a numeric partial differential equation solver (MATLAB) applied to the device geometry (Fig. S3 (a)).

The spatially-varying electron temperature is described by the two-dimensional heat equation

$$\dot{q}(r) = -\nabla \cdot [\kappa(r) \nabla T_e(r)] + \Sigma_{ep}[T_e^{\delta} - T^{\delta}] \,, \text{(S.3)}$$

where $\dot{q}(r)$ is the power per unit area absorbed by the electrons at position *r*, $\kappa(r)$ is the spatially-varying thermal conductivity, $\Sigma_{ep}$ is the electron-phonon coupling constant, $T$ is the phonon (device) temperature, and $\delta$ is an exponent that describes the electron-phonon coupling and is typically equal to 3. The first term on the right-hand side describes diffusive motion of the electrons, which allows heat to dissipate by diffusion into the contacts, and the second term describes heat loss to phonons. The electron thermal conductivity is given by the Wiedemann-Franz law,

$$\kappa(r) = \frac{\pi^2}{3}\left(\frac{k}{e}\right)\sigma T_e(r) \,. \text{(S.4)}$$

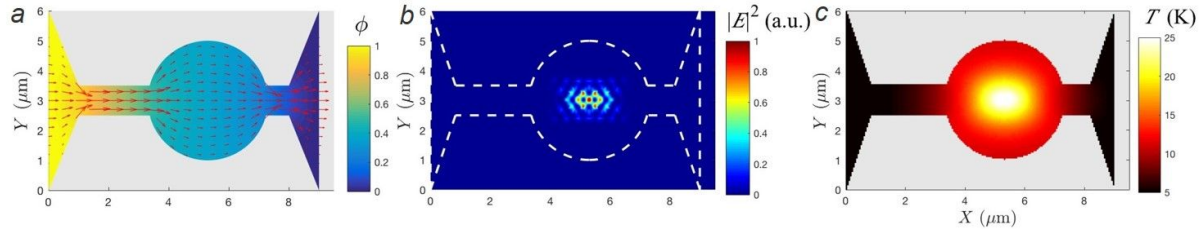


**Figure S3: Numeric evaluation of the Johnson noise temperature.** (a) The weighting function $\phi(r)$, which is given by a solution to the Laplace equation with the source set to $\phi = 1$ and the drain set to $\phi = 0$. Red arrows show the gradient - $\vec{\nabla}\phi(r)$. (b) The intensity of the cavity mode as a function of position. The relative position of the graphene sample is illustrated with dashed white lines. (c) Numerical solution for the spatially-varying electron temperature $T_e(r)$, assuming an absorbed power *P*=20 nW and a base temperature *T* = 5 K.

The heating of electrons comes predominantly from the cavity mode, so that $\dot{q}(r)$ is proportional to the squared electric field of the cavity. We therefore write $\dot{q}(r) = P f_c(r)$, where *P* is the total power absorbed and $f_c(r)$ is a distribution function that is proportional to the squared electric field in the cavity mode and which integrates to unity, $\int f_c(r) d^2 r = 1$. The cavity mode profile $f_c(r)$ is calculated numerically using Lumerical, and is plotted in Fig. S3 (b). In principle, there is a small amount of additional power that is absorbed directly by graphene electrons from the laser spot, independently of the cavity mode. This additional absorption is small compared to the absorption from the cavity mode, and does not noticeably alter our results. In principle, however, it can be added to the function $\dot{q}(r)$.

If the electron-phonon coupling constant $\Sigma_{ep}$ is known, then we can solve Eqn. (S.3) numerically to determine the electron temperature $T_e(r)$ as a function of position. This is done numerically, with the boundary conditions $T_e = T$ at the contacts (which are good heat absorbers due to their high electronic density of states) and reflecting boundary conditions at the other edges of the sample. An example for the solution $T_e(r)$ is shown in Fig. S3 (c).

Once $T_e(r)$ is known, the Johnson Noise temperature $T_{JN}$ can be calculated using equation (S.2).

The value of the constant $\Sigma_{ep}$ for our device is not known *a priori*. We infer $\Sigma_{ep}$ by fitting our measured data for $T_{JN}$ versus $P$, as shown in Fig. 3(a) of the main text, which gives $\Sigma_{ep} \approx 0.038$ and $\delta \approx 3.0$.

Finally, we can also use our numerical modeling to describe the variation in the Johnson noise temperature as a function of the position of the laser spot. For this calculation we assume that the power in the cavity mode is proportional to the laser power multiplied by the spatial overlap between the laser spot profile and the cavity mode profile. That is,

$$\dot{q}(r) = P_0 f_c(r) \int f_c(r') f_l(r') d^2 r' \text{ , (S.5)}$$

where $P_0$ is proportional to the laser power and $f_l(r)$ is a Gaussian distribution that describes the laser spot intensity. In our modeling we assume a beam spot width 1.5 $\mu m$. An example calculation of the resulting Johnson noise $T_{JN}$ as a function of the beam spot position is given in Fig. S3.

Equation (S.5) can be justified theoretically by considering a generalization of the Breit-Wigner model for coupling of a continuous excitation (here, light) to a resonant excitation (here, the photonic cavity mode)[2]. In particular, if light with energy $\omega$ is coupled to a resonant excitation mode with energy $\omega_0$ and damping $\gamma$, then the absorption coefficient

$$A = \frac{4\Gamma\gamma}{(\omega - \omega_0)^2 + (\Gamma + \gamma)^2} \text{ . (S.6)}$$

Here, $\Gamma$ represents the resonance width, and in our problem the damping $\gamma$ arises from coupling between the cavity mode and the graphene electrons. In the traditional Breit-Wigner problem, $\Gamma = \nu g^2$, where $\nu$ is the density of states for the continuous excitation and *g* is the coupling constant between the resonant mode and the free photons. In our problem, the coupling constant *g*(*r*) at a given spatial location *r* is proportional to the magnitude of the local electric field $E(r)$ in the cavity mode. By Eq. (S.6), we therefore have a local absorption coefficient *A*(*r*) that is proportional to the square of the cavity mode electric field, $A(r) \propto |E(r)|^2 \propto f_c(r)$.

We arrive at Eq. (S.5) by defining the total power in the cavity mode as the integral of the local laser power $P(r) \propto f_l(r)$ multiplied by the local absorption coefficient *A*(*r*). One can note that in doing so we ignore the potential coupling between free photon modes emitted at different spatial locations of the sample. Such coupling can be expected to be small so long as the integrated absorption coefficient is small compared to unity.


[1] J. C. W. Song and L. S. Levitov, Phys. Rev. B Condens. Matter **90**, 075415 (2014).

[2] L. D. Landau, E. M. Lifshitz, J. B. Sykes, J. S. Bell, and M. E. Rose, Phys. Today **11**, 56 (1958).